



Article

Enhanced Visible-Light Photocatalytic Performance of SAPO-5-Based g-C₃N₄ Composite for Rhodamine B (RhB) Degradation

Lingfang Qiu ¹, Zhiwei Zhou ¹, Mengfan Ma ¹, Ping Li ¹ , Jinyong Lu ¹, Yingying Hou ¹, Xiangshu Chen ² and Shuwang Duo ^{1,*} 

¹ Jiangxi Key Laboratory of Surface Engineering, Jiangxi Science and Technology Normal University, Nanchang 330013, China; qlf1108@163.com (L.Q.); pharmacy_zhou@163.com (Z.Z.); MF1783975@126.com (M.M.); lp1849065552@163.com (P.L.); ljy1873642671@163.com (J.L.); hyy18170401838@163.com (Y.H.)

² Institute of Advanced Materials (IAM), State-Province Joint Engineering Laboratory of Zeolite Membrane Materials, College of Chemistry and Chemical Engineering, Jiangxi Normal University, Nanchang 330022, China; cxs66cn@jxnu.edu.cn

* Correspondence: swduo@imr.ac.cn; Tel.: +86-79183831266; Fax: +86-79183831266

Received: 4 November 2019; Accepted: 26 November 2019; Published: 28 November 2019



Abstract: Novel visible-light responded aluminosilicophosphate-5 (SAPO-5)/g-C₃N₄ composite has been easily constructed by thermal polymerization for the mixture of SAPO-5, NH₄Cl, and dicyandiamide. The photocatalytic activity of SAPO-5/g-C₃N₄ is evaluated by degrading RhB (30 mg/L) under visible light illumination ($\lambda > 420$ nm). The effects of SAPO-5 incorporation proportion and initial RhB concentration on the photocatalytic performance have been discussed in detail. The optimized SAPO-5/g-C₃N₄ composite shows promising degradation efficiency which is 40.6% higher than that of pure g-C₃N₄. The degradation rate improves from 0.007 min⁻¹ to 0.022 min⁻¹, which is a comparable photocatalytic performance compared with other g-C₃N₄-based heterojunctions for dye degradation. The migration of photo-induced electrons from g-C₃N₄ to the Al site of SAPO-5 should promote the photo-induced electron-hole pairs separation rate of g-C₃N₄ efficiently. Furthermore, the redox reactions for RhB degradation occur on the photo-induced holes in the g-C₃N₄ and Al sites in SAPO-5, respectively. This achievement not only improves the photocatalytic activity of g-C₃N₄ efficiently, but also broadens the application of SAPOs in the photocatalytic field.

Keywords: g-C₃N₄; SAPO-5; composite; photocatalytic; visible light

1. Introduction

For the society's development and rapid industrialization, environmental pollution becomes much more serious. Noticeably, water purification requiring advanced technologies draws much attention in the research community. Photocatalysis is regarded as a superior approach for water treatment because of its unique advantages, such as non-secondary pollution, simple operation, short reaction period, and mild environment.

Graphitic carbon nitride (g-C₃N₄), a novel polymeric semiconductor, has become a new generation in the photocatalytic arena. Meaningful, characters like visible-light (over 43% of the solar energy) response, low cost, and ultrahigh physicochemical stability are believed to make g-C₃N₄ attractive for researchers. However, the mortal shortage, namely the narrow band gap energy (2.7 eV) leading to quick photo-induced electron-hole pair recombination, hinders the practical application of g-C₃N₄ [1]. Thus, g-C₃N₄-based heterojunction with resembled band structure promotes many urgent questions.

Many semiconductors with a wider band gap have been applied in constructing g-C₃N₄-based heterojunctions, such as traditional TiO₂ [2], ZnO [3], CdS [4], and so on.

Zeolites or zeolitic materials, a big family of porous materials, show many distinct properties, such as framework component controllability and high adsorption. Aluminosilicates and aluminosilicophosphates (SAPOs) are usually used as catalysts in cracking, isomerization, and alkylation reactions, such as SAPO-34 [5,6], Y-type [7,8], and ZSM-5 [9]. Recently, it was found that aluminosilicates and SAPOs also exhibited photocatalytic activity for the charge transfer excited state of [Al²⁺-O⁻]* under UV illumination, which has been demonstrated in some literature [9,10]. SAPO-5 has successfully been used as a direct photocatalyst for CO₂ energy conversion and organic pollutant degradation owing to the special electron transfer pattern within activated [Al²⁺-O⁻]* sites where Al behaves as the electron acceptor and O acts as the electron donor. Furthermore, SAPO-5 has been applied in heterojunction-like construction with TiO₂ [11], but the photocatalytic performance still needs to be improved and the photocatalytic mechanism is still not very clear.

In our previous study, SAPO-5 with a high ratio of Si/Al and nanometer-sized particles (high-silica SAPO-5) was found to have good photocatalytic activity under UV illumination for vast active sites [12]. Herein, we propose to construct a novel heterojunction-like composite by combining as-synthesized high-silica SAPO-5 with g-C₃N₄ nanosheet. Photodegradation for rhodamine B (RhB) will be chosen as the model to evaluate the photocatalytic activity of SAPO-5/g-C₃N₄. As far as we know, it is the first time modifying g-C₃N₄ with SAPO-5. The effects of SAPO-5 incorporation proportion and initial RhB solution concentration on the physicochemical properties and optical properties of SAPO-5/g-C₃N₄ will be analyzed by a series of characterizations and photodegradation pattern will be discussed in detail. Finally, the RhB degradation mechanism of SAPO-5/g-C₃N₄ will be proposed.

2. Experimental

2.1. Materials

Ammonium chloride (Damao Chemical Reagent Factory, Tianjin, China), dicyandiamide (Sinopharm Chemical Reagent Co., Ltd., Shanghai, China), ultra-pure water (made in the lab), and rhodamine B (Aladdin, Shanghai, China) were used in the following experiments.

2.2. Synthesis of SAPO-5/g-C₃N₄ Composite

SAPO-5/g-C₃N₄ composites were prepared simply by co-thermal polymerization. High-silica SAPO-5 has already been made in our laboratory and we use as-synthesized high-silica SAPO-5 directly in the subsequent experiments. Pure g-C₃N₄ nanosheet marked as CN-0 was synthesized according to the literature [13]. Typically, 15 g of NH₄Cl and 3 g of dicyandiamide were dissolved in 50 mL ultra-pure water and then the mixture was evaporated at 80 °C under stirring until dry white solids formed again. Later, the mixture was transferred to a crucible with a cover and calcined at 500 °C for 4 h in a muffler. Either the heating rate or the cooling rate is 2 °C/min. To fabricate SAPO-5/g-C₃N₄ composite, SAPO-5 crystals were added into a mixture containing water, NH₄Cl, and dicyandiamide, as described above. The mass ratios of SAPO-5 and the precursor of g-C₃N₄ were adjusted from 0% to 0.11%, 0.44%, 1.67%, 2.78%, 4.44%, and 5.56%, respectively. It should be noted that other treatments compared with pure g-C₃N₄ preparation were not changed. The final SAPO-5/g-C₃N₄ composites with different component contents (Table S1) were marked as SAPO-5/g-C₃N₄-X (X = 1, 2, 3, 4, 5, 6), successively.

2.3. Characterization

X-ray diffraction (XRD) (Shimadzu XRD-6100, Kyoto, Japan) was used for confirming the crystal phase of samples. A scanning electron microscope (SEM) (Zeiss Sigma, Jena, Germany) was applied to investigating the microstructure of samples and the contact surface between the SAPO-5 and g-C₃N₄ nanosheets in low resolution. The transmission electron microscope (TEM) (Tecnai G220

S-TWIN, Hillsboro, RO, USA) provides microstructure images with a much higher resolution of the $g\text{-C}_3\text{N}_4$ nanosheet and the SAPO-5/ $g\text{-C}_3\text{N}_4$ hybrid structure. Surface groups of samples were detected by Fourier transform infrared spectroscopy (FT-IR) (Spectrometer PerkinElmer Spectrum Two, Waltham, MA, USA). UV-visible diffuse reflection spectra (DRS) (EscalLab 250 Xi, Shanghai, China), photoluminescence (PL) (Zolix LSP-X500A, Beijing, China), photocurrent (CHI660E, Shanghai, China), X-ray photoelectron spectroscopy (XPS) (ThermoFisher K-Alpha, Shanghai, China), and time-resolved fluorescence spectra (C11367, Quantaaurus-Tau, Hamamatsu, Japan) were applied for analyzing a series of optical properties of the photocatalysts, which will be discussed below in detail.

2.4. Photocatalytic Experiment

Visible-light photocatalytic experiments were carried out within an optical reaction apparatus (XPA Xujiang, Nanjing, China) using a xenon lamp with a power of 500 W to produce visible radiation. The photocatalysts were applied to a degrading RhB aqueous solution. The physical adsorption equilibrium was achieved after 1 h in a dark environment. After that, the xenon lamp was turned on and samples were extracted every 20 min. The absorbance of dye solution after centrifugation was marked as A , which is proportional to dye concentration C . The initial absorbance and dye concentration were A_0 and C_0 , respectively.

3. Results and Discussion

3.1. Characterization of Samples

Figure 1 showed the XRD patterns of pure $g\text{-C}_3\text{N}_4$, SAPO-5, and SAPO-5/ $g\text{-C}_3\text{N}_4$ composites with different SAPO-5 incorporation proportions. The pattern for $g\text{-C}_3\text{N}_4$ indicated that pure $g\text{-C}_3\text{N}_4$ was prepared successfully, and the main peak located at $2\theta = 27.7^\circ$ represented the (002) plane of $g\text{-C}_3\text{N}_4$, which agreed well with the data reported [14]. In addition, the interlayer stacking of synthesized $g\text{-C}_3\text{N}_4$ was 0.322 nm, which was similar to previously reported $g\text{-C}_3\text{N}_4$ [13]. All peaks in the XRD pattern of SAPO-5 were totally in tune with the typical peaks of pure SAPO-5 in reports [10,15]. After composites of SAPO-5/ $g\text{-C}_3\text{N}_4$ were formed, the XRD patterns became the combination of pure $g\text{-C}_3\text{N}_4$ and SAPO-5. According to the corresponding patterns, we found that when the incorporation proportion of SAPO-5 was too small, it was difficult to detect the SAPO-5 crystal phase. As the incorporation proportion increased, the intensity of $g\text{-C}_3\text{N}_4$ was covered by SAPO-5, generally. Moreover, there was no impurity formed during the synthesis process of the composite photocatalysts, and the crystallinity of SAPO-5 was maintained perfectly.

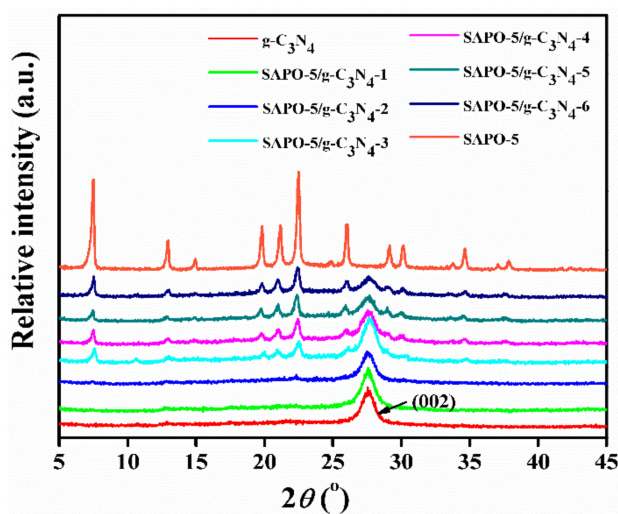


Figure 1. XRD patterns of pure $g\text{-C}_3\text{N}_4$ and aluminosilicophosphate-5 (SAPO-5)/ $g\text{-C}_3\text{N}_4$ composites with different SAPO-5 incorporation proportions and pure SAPO-5.

FT-IR spectra were applied for confirming the components of synthesized samples. As shown by the spectrum of pure $g\text{-C}_3\text{N}_4$ in Figure 2, the obvious peak at 810 cm^{-1} was from the stretching vibration of tri-s-triazine rings [16,17]. The strong peaks located within the range $1650\text{--}1200\text{ cm}^{-1}$ originated from the stretching vibration of aromatic C–N heterocycles [18,19]. The broad peaks representing the stretching vibration of NH groups were at $3000\text{--}3400\text{ cm}^{-1}$ [20]. Based on these distinctive peaks, it was demonstrated that $g\text{-C}_3\text{N}_4$ was indeed formed. Moreover, it should be noticed that the peak at 1640 cm^{-1} came from the unavoidable physical adsorption of O–H [21]. For pure SAPO-5, the corresponding spectrum indicated that peaks at 475 cm^{-1} , 1115 cm^{-1} , and 3486 cm^{-1} were assigned to the benching vibration of primary structural units (like SiO_4 and AlO_4), the stretching vibration of Si–O–Si, and the presence of P–OH, respectively [22,23]. It was obvious that during the formation of the SAPO-5/ $g\text{-C}_3\text{N}_4$ composites, the component of $g\text{-C}_3\text{N}_4$ was well maintained. Furthermore, the peaks of SAPO-5 appeared as the incorporation proportion increased, which was well in accordance with Figure 1. It can be determined that SAPO-5 has been closely integrated with $g\text{-C}_3\text{N}_4$.

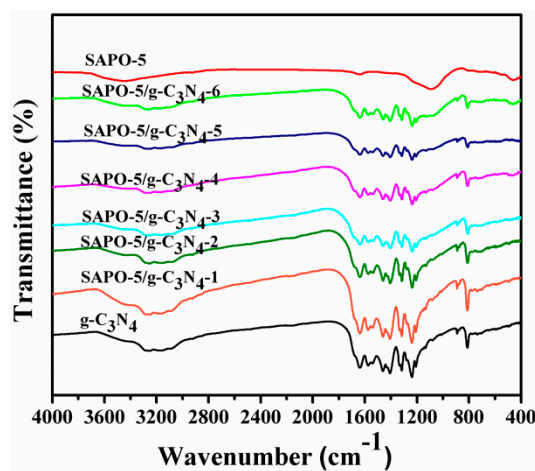


Figure 2. FT-IR patterns of pure $g\text{-C}_3\text{N}_4$ and SAPO-5/ $g\text{-C}_3\text{N}_4$ composites with different SAPO-5 incorporation proportions and pure SAPO-5.

Figure 3 shows SEM images of pure SAPO-5 and pure $g\text{-C}_3\text{N}_4$ (Figure 3a,b), and SEM image and TEM images of SAPO-5/ $g\text{-C}_3\text{N}_4$ (Figure 3c,d), respectively. Obviously, SAPO-5 nanoparticles, with a particle size of 30–60 nm spread all over the $g\text{-C}_3\text{N}_4$ nanosheets, can effectively retard the aggregation of $g\text{-C}_3\text{N}_4$. The TEM image displays the intimate contact between nanometer-sized SAPO-5 particles and ultrathin transparent $g\text{-C}_3\text{N}_4$, which indicates the formation of a hybrid structure facilitating and improving the photocatalytic activity of $g\text{-C}_3\text{N}_4$.

The chemical bonds in pure $g\text{-C}_3\text{N}_4$ and SAPO-5/ $g\text{-C}_3\text{N}_4$ -4 were measured by X-ray photoelectron spectroscopy (XPS), and the results were illustrated in Figure 4. The full spectrum (Figure 4a) indicated that C, N, O, and Al from SAPO-5 exist in the sample. Deeper analysis for heterojunction-like construction was carried out based on the spectra for C 1s, N 1s, O 1s, and Al 2p. All the peaks were calibrated by C 1s peak at 284.6 eV. For C 1s spectra (Figure 4b), compared with pure $g\text{-C}_3\text{N}_4$, the formation of C–O located at 286.1 eV of SAPO-5/ $g\text{-C}_3\text{N}_4$ -4 indicated the chemical contact between $g\text{-C}_3\text{N}_4$ and SAPO-5. Moreover, from the spectra of C 1s, N 1s, and O 1s it was obvious that C–C, N–C=N, pyridine N, pyrrole N, graphitic N, and O–H bonds existed in pure $g\text{-C}_3\text{N}_4$ and SAPO-5/ $g\text{-C}_3\text{N}_4$ -4 [24]. Furthermore, the binding energies of these bonds were all higher in SAPO-5/ $g\text{-C}_3\text{N}_4$ -4, which showed that the electron cloud density was lower in $g\text{-C}_3\text{N}_4$ and in SAPO-5/ $g\text{-C}_3\text{N}_4$ -4 compared with pure $g\text{-C}_3\text{N}_4$. In addition, the Al 2p binding energy in SAPO-5/ $g\text{-C}_3\text{N}_4$ -4 was lower than that in pure SAPO-5, which indicated that the electron cloud density in SAPO-5/ $g\text{-C}_3\text{N}_4$ -4 was higher than that in pure SAPO-5. Based on the above analysis, we can estimate that the photo-induced electrons move

from $g\text{-C}_3\text{N}_4$ to the Al sites in SAPO-5 for SAPO-5/ $g\text{-C}_3\text{N}_4$ -4, which should facilitate the separation of photo-induced electron-hole pairs in $g\text{-C}_3\text{N}_4$.

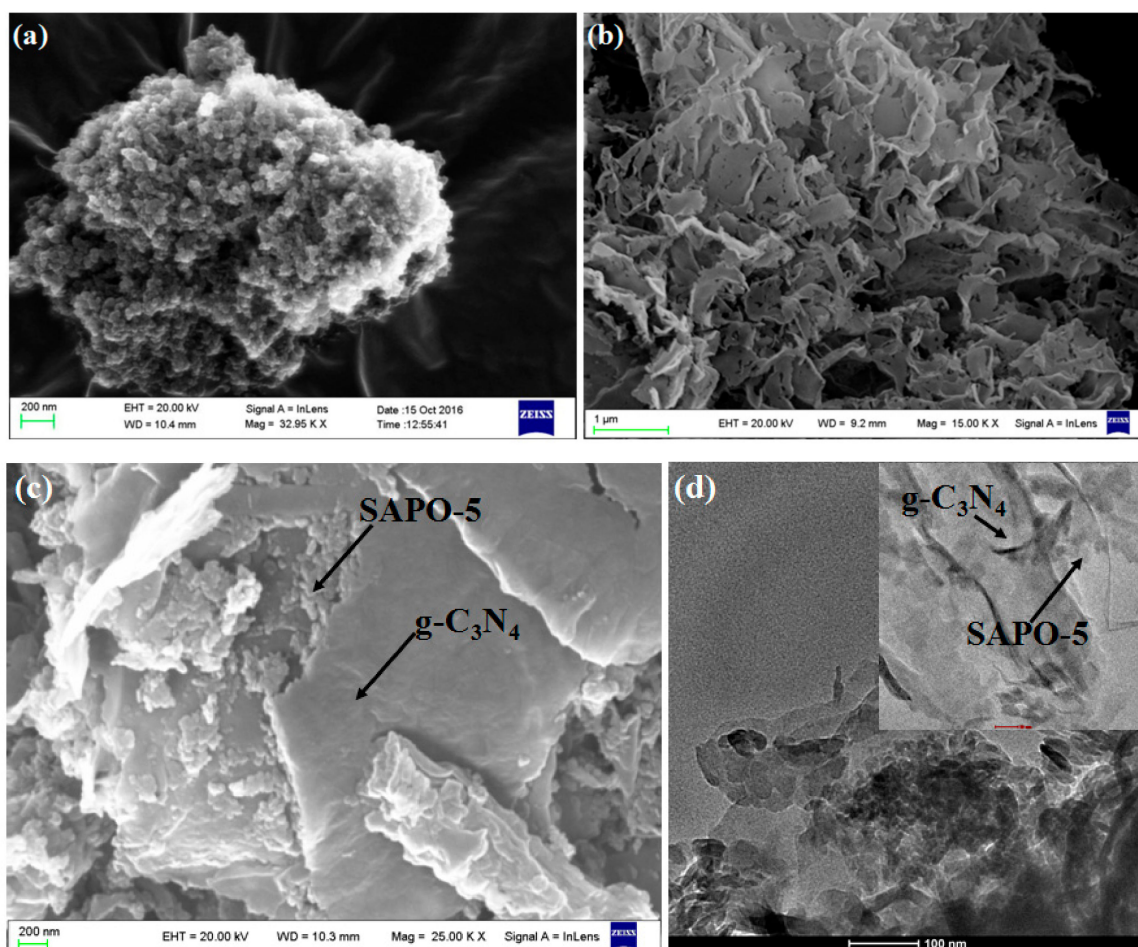


Figure 3. SEM images of pure SAPO-5 (a), pure $g\text{-C}_3\text{N}_4$ (b), and SAPO-5/ $g\text{-C}_3\text{N}_4$ -4 composite (c); and the TEM image of SAPO-5/ $g\text{-C}_3\text{N}_4$ -4 (d) (the inset in (d) is the TEM image under higher resolution).

The diffuse reflectance spectra (DRS) within a wavelength range of 200 nm to 800 nm for the synthesized composites and pure $g\text{-C}_3\text{N}_4$ are shown in Figure 5a. Obviously, the adsorption edges of the samples were similar, but when incorporating a small amount of SAPO-5 particles, the composites showed higher absorbance in the visible light range (inset in Figure 5a). When the amount of SAPO-5 was higher than 0.5 g, the absorbance decreased compared with pure $g\text{-C}_3\text{N}_4$. Obviously, a certain amount of SAPO-5 particles inhibited the aggregation of $g\text{-C}_3\text{N}_4$ effectively, which improved the absorption ability of visible light in $g\text{-C}_3\text{N}_4$. As the amount increased, the insulation property of SAPO-5 limited the absorption ability of visible light in $g\text{-C}_3\text{N}_4$ undesirably. In addition, band gaps of the samples were calculated according to the Tauc plot (where α , h , and ν were the linear absorption coefficient, Planck constant, and light frequency, respectively) [25]. The constant of 1/2 was adopted for the samples. Figure 5b shows a band gap comparison between pure $g\text{-C}_3\text{N}_4$ (2.61 eV) and SAPO-5/ $g\text{-C}_3\text{N}_4$ -4 (2.65 eV). Due to the dispersion of SAPO-5, the band gap of synthesized composites became larger, which should be attributed to the large band gap for most zeolites. Nevertheless, it demonstrated that the hybrid structures of SAPO-5/ $g\text{-C}_3\text{N}_4$ have been formed successfully.

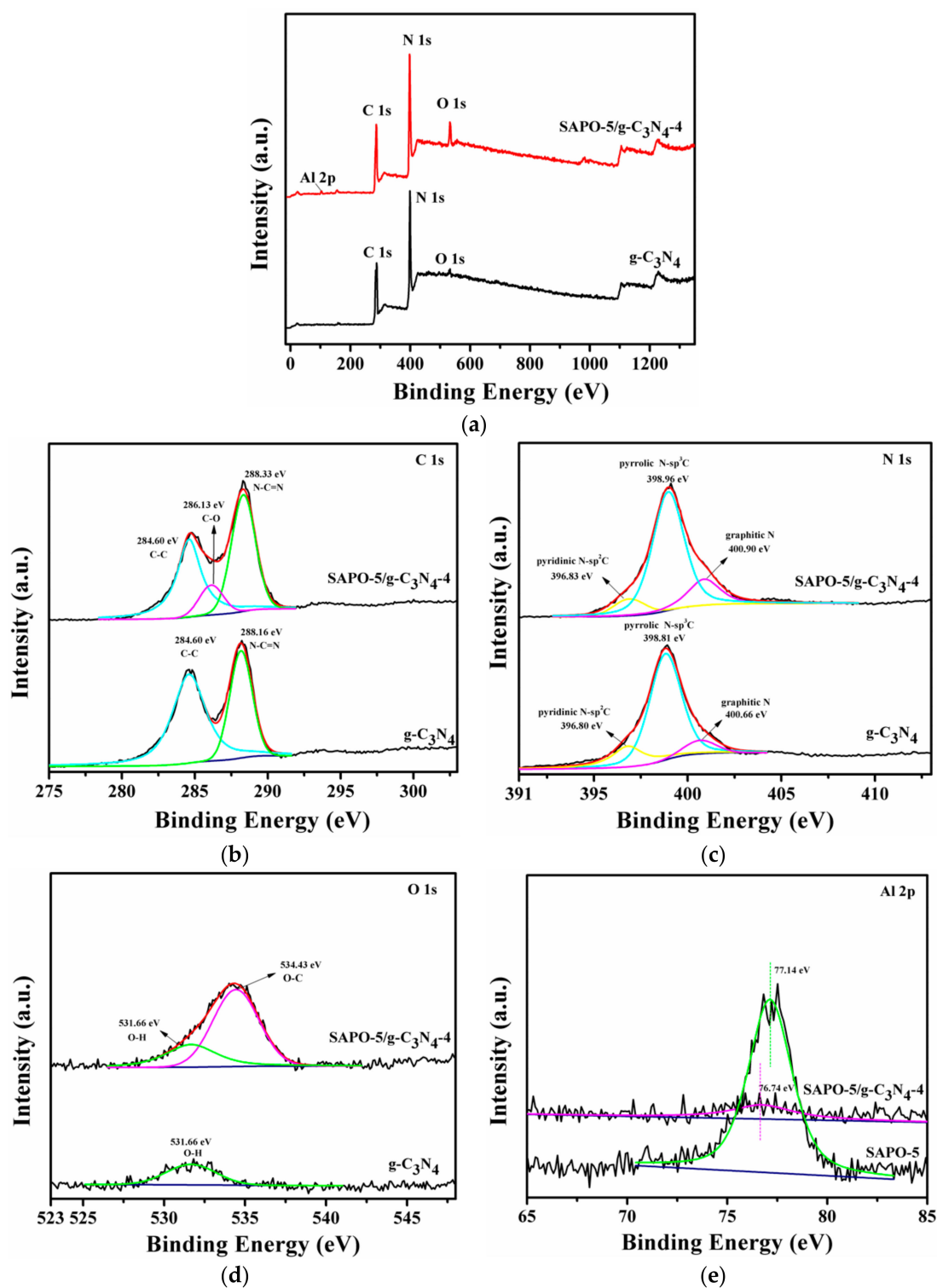


Figure 4. X-ray photoelectron spectroscopy (XPS) spectra of the survey (a), C 1s (b), N 1s (c), and O 1s (d) of pure $g\text{-C}_3\text{N}_4$ and SAPO-5/ $g\text{-C}_3\text{N}_4$ -4, and XPS spectra of Al 2p (e), pure SAPO-5, and SAPO-5/ $g\text{-C}_3\text{N}_4$ -4.

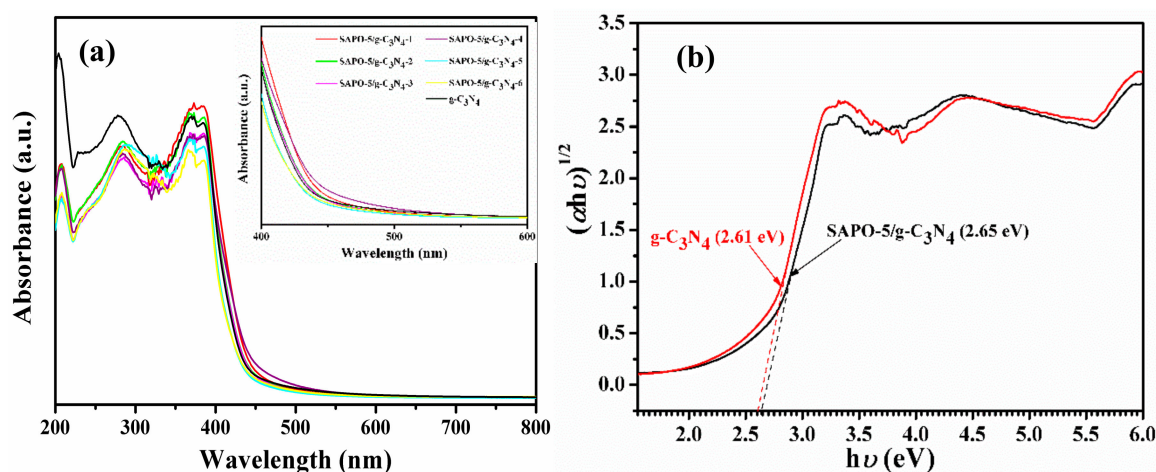


Figure 5. UV-vis diffuse reflection spectra (DRS) of pure $g\text{-C}_3\text{N}_4$ and SAPO-5/ $g\text{-C}_3\text{N}_4$ composites with different SAPO-5 incorporation proportions (a), and plots of $(\alpha h\nu)^{1/2}$ versus $h\nu$ for the band gap energy of pure $g\text{-C}_3\text{N}_4$ and SAPO-5/ $g\text{-C}_3\text{N}_4$ -4 (b).

Photoluminescence (PL) at room temperature is always applied when evaluating the charge recombination rate of photocatalysts. Higher intensity means a faster charge recombination rate, in theory [18]. Figure 6 indicates that after adding SAPO-5, the photo-induced electron-hole pairs of $g\text{-C}_3\text{N}_4$ can be separated much more effectively. As expected, the separation efficiency was affected by the incorporation proportion of SAPO-5. When the incorporation proportion was 0.5 g, $g\text{-C}_3\text{N}_4$ /SAPO-5 showed the most preferable charge transferability, which further verified the formation of a hybrid structure of SAPO-5/ $g\text{-C}_3\text{N}_4$.

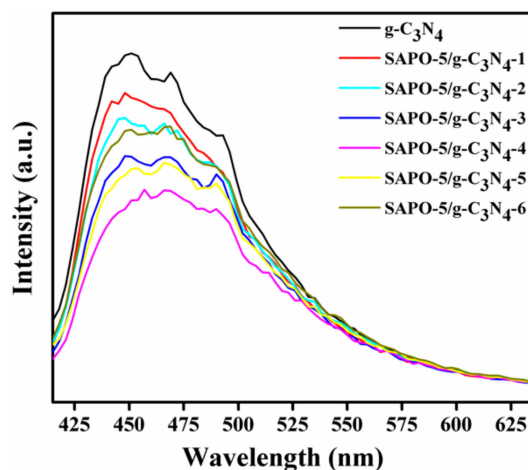


Figure 6. The photoluminescence (PL) spectra of pure $g\text{-C}_3\text{N}_4$ and SAPO-5/ $g\text{-C}_3\text{N}_4$ composites with different SAPO-5 incorporation proportions.

It is meaningful to use photocurrent to evaluate the photo-induced electron density of activated photocatalysts. As shown in Figure 7, compared to pure $g\text{-C}_3\text{N}_4$, it was obvious that SAPO-5/ $g\text{-C}_3\text{N}_4$ had a stronger electric current when the light was turned on. Naturally, the electric current decreased sharply and disappeared finally when the light was turned off.

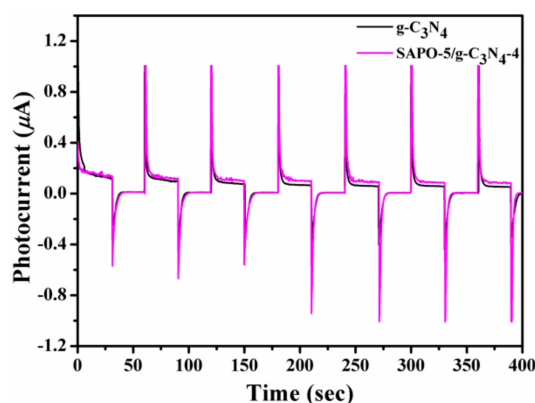


Figure 7. The photocurrent patterns of pure $g\text{-C}_3\text{N}_4$ and SAPO-5/ $g\text{-C}_3\text{N}_4$ -4.

The separation efficiency of photo-induced carriers is one of the most critical issues during the investigation of photocatalysts. Time-resolved fluorescence was applied when recording the photo-induced carrier separation processes of pure $g\text{-C}_3\text{N}_4$ and SAPO-5/ $g\text{-C}_3\text{N}_4$ -4 (Figure 8). The fluorescence times of pure $g\text{-C}_3\text{N}_4$ and SAPO-5/ $g\text{-C}_3\text{N}_4$ were 3.0 ns and 4.4 ns, respectively. As discussed in our previous publication, SAPO-5 can hardly be activated under 380 nm [12], thus, we can suppose that SAPO-5/ $g\text{-C}_3\text{N}_4$ -4 showed a much higher photo-induced carrier separation rate than pure $g\text{-C}_3\text{N}_4$. This should have made many contributions to the photocatalytic performance of the samples.

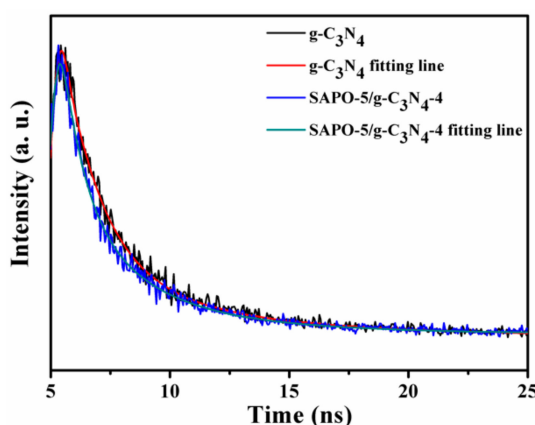


Figure 8. The time-resolved fluorescence decay spectra of pure $g\text{-C}_3\text{N}_4$ and SAPO-5/ $g\text{-C}_3\text{N}_4$ -4.

3.2. Visible-Light Photocatalytic Performance

The photocatalytic activity of catalysts is affected by many factors. Herein, we first discussed the role of dye concentration in the photocatalytic process of the samples to explore an appropriate environment reflecting the higher photocatalytic potential of photocatalysts.

3.2.1. Effect of Initial RhB Concentration

The initial RhB concentrations were fixed on 10 mg/L, 30 mg/L, and 50 mg/L, respectively. As shown in Figure 9a, the photocatalytic activities of pure $g\text{-C}_3\text{N}_4$ and composite SAPO-5/ $g\text{-C}_3\text{N}_4$ -4 were affected significantly as the concentration increased, especially when RhB concentration was 50 mg/L. For pure $g\text{-C}_3\text{N}_4$, the degradation efficiency decreased from 89.05% to 21.45% sharply. However, for SAPO-5/ $g\text{-C}_3\text{N}_4$ -4, the degradation efficiencies were similar under the RhB concentrations of 10 mg/L (91.63%) and 30 mg/L (94.74%), while it decreased to 33.12% when the RhB concentration increased to 50 mg/L. In general, photocatalysts with the same amount of active sites can't decompose too many extra organic composites in higher RhB concentration, which was in accordance with the behavior of pure $g\text{-C}_3\text{N}_4$. In comparison, composite SAPO-5/ $g\text{-C}_3\text{N}_4$ -4 still behaved well in RhB with a

higher concentration of 30 mg/L, which was likely due to the sufficient amount of active sites which were superfluous in the RhB solution with a small concentration of 10 mg/L. Thus, 30 mg/L was an optimum concentration to exhibit the superior photocatalytic activity of SAPO-5/g-C₃N₄-4 compared to pure g-C₃N₄. The corresponding plots obtained from the UV-vis spectrophotometer can be seen in Figure S1.

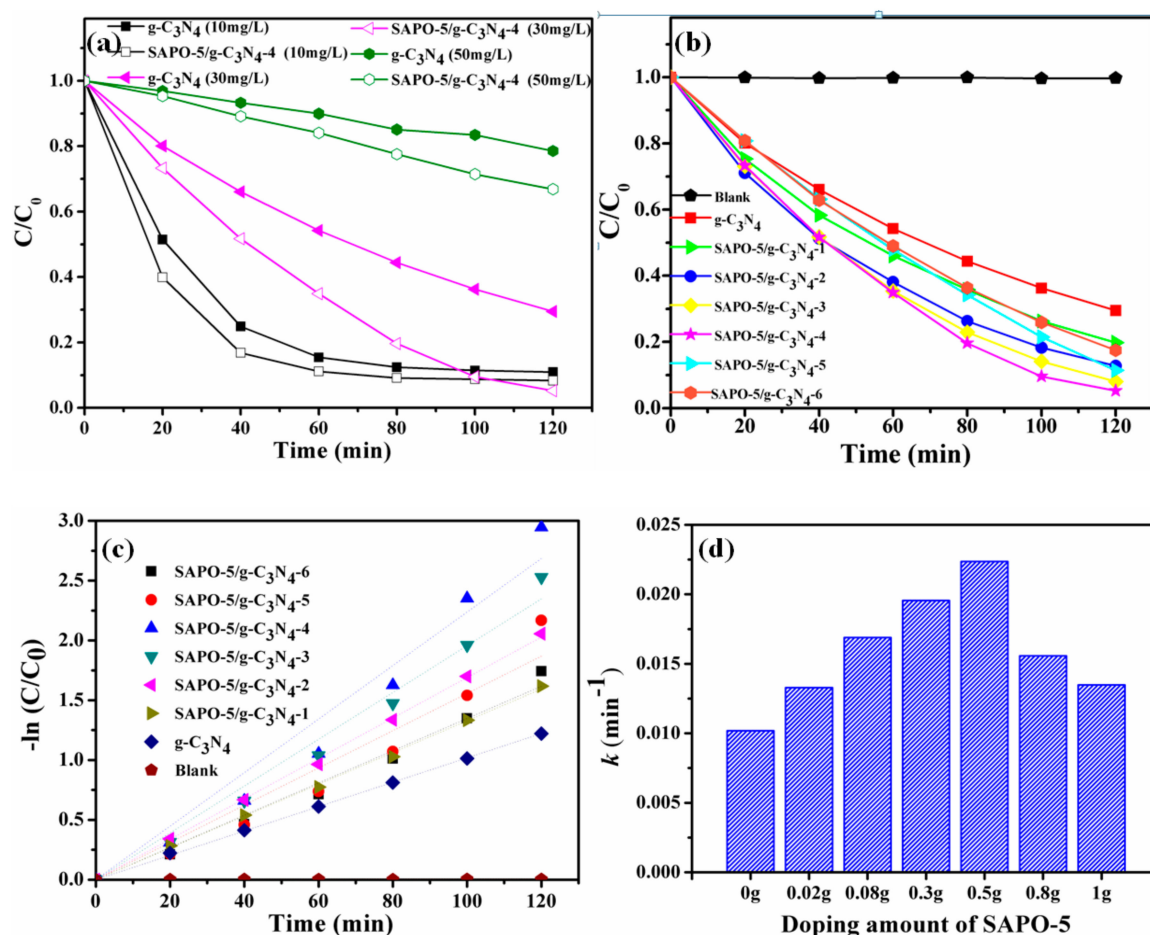


Figure 9. The photocatalytic performances for RhB degradation in the presence of g-C₃N₄ and SAPO-5/g-C₃N₄-4 under different RhB concentrations (a) ([RhB]_{initial}: 10–50 mg/L, catalyst dose: 50 mg, volume: 50 mL, reaction time: 120 min, light source: Xenon lamp, 500 W, $\lambda > 420$ nm), photocatalytic performances (b), pseudo-first-order kinetic plots (c), and reaction rate constant (d) for RhB degradation in the presence of g-C₃N₄ and SAPO-5/g-C₃N₄ composites with different SAPO-5 incorporation proportions ([RhB]_{initial}: 30 mg/L, catalyst dose: 50 mg, volume: 50 mL, reaction time: 120 min, light source: Xenon lamp, 500 W, $\lambda > 420$ nm).

3.2.2. Effect of the SAPO-5 Incorporation Proportion

After optimizing the proper RhB concentration, the best SAPO-5 incorporation proportion was screened for SAPO-5/g-C₃N₄ to exhibit higher RhB degradation performance. As shown in Figure 9b, the RhB degradation efficiencies increased remarkably after they were incorporated with SAPO-5. When the SAPO-5 incorporation proportion is 0.5 g, the degradation efficiency increased from 70.52% to 94.74%, which is 34.34% higher than pure g-C₃N₄. To confirm that RhB didn't degrade itself, a blank experiment was carried out and the degradation efficiency was only 0.27%. In addition, Figure 9c,d indicated that the degradation rate constant increased from 0.013 min⁻¹ to 0.022 min⁻¹ compared with pure g-C₃N₄ (Table S2). The corresponding plots obtained from the UV-vis spectrophotometer can also be seen in Figure S2.

To further evaluate the photocatalytic activity quantitatively, it is necessary to analyze the synergistic factor (SF) in the composites, which is based on the following equation [26]:

$$SF = \frac{k_{g-C_3N_4/SAPO-5(X:Y)}}{k_{SAPO-5} \times (1 - X) + k_{g-C_3N_4} \times X} \quad (1)$$

where $k_{g-C_3N_4/SAPO-5}$, k_{SAPO-5} , $k_{g-C_3N_4}$ are the photodegradation rates of SAPO-5/g-C₃N₄, SAPO-5, and pure g-C₃N₄ for RhB degradation (30 mg/L) under visible illumination (Figure 9d). X and Y are the contents of SAPO-5 and pure g-C₃N₄ in the SAPO-5/g-C₃N₄ composites (Table S1). Obviously, k_{SAPO-5} is regarded as zero because SAPO-5 can hardly have photocatalytic activity (Table S2). All the composites show a synergistic effect because the synergistic factors are all larger than 1.00. Moreover when SAPO-5 content is 30.25%, SAPO-5/g-C₃N₄ shows the greatest synergistic effect leading to the highest RhB degradation in this work.

3.3. Reusability

Five-time cyclic experiments have been carried out to confirm the stability of SAPO-5/g-C₃N₄-4. As shown by Figure 10, it turned out that SAPO-5/g-C₃N₄-4 showed good stability during RhB degradation under visible light illumination. To further demonstrate that conclusion, SAPO-5/g-C₃N₄-4, after the 5th recycling, was characterized by XRD and SEM (Figures S3 and S4). As expected, both the crystal phase and microstructure remained unchanged during the whole experiment.

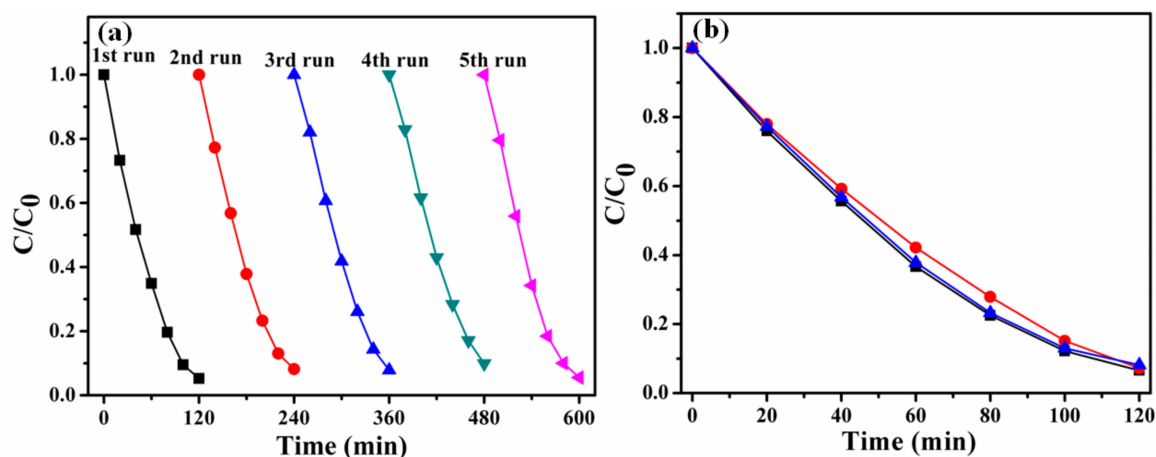


Figure 10. The recycling results of the photocatalytic performance of SAPO-5/g-C₃N₄-4 for RhB degradation (a) and the stability of preparing SAPO-5/g-C₃N₄-4 evaluated by RhB degradation (b) ([RhB]_{initial}: 30 mg/L, catalyst dose: 50 mg, volume: 50 mL, reaction time: 120 min, light source: Xenon lamp, 500 W, $\lambda > 420$ nm).

Moreover, synthesis reproducibility of photocatalysts is critical for practical application. SAPO-5/g-C₃N₄-4 have been synthesized several times and applied to the photodegradation for RhB. As Figure 10b showed, this sample can easily be synthesized and shows similar photocatalytic activity, which indicates the ideal synthesis reproducibility of SAPO-5/g-C₃N₄-4.

3.4. Synergistic Photocatalytic Degradation Mechanism

Investigation on the crucial active species during the photocatalytic process using as-synthesized SAPO-5/g-C₃N₄-4 is very important for proposing the photocatalytic degradation mechanism. Trapping agents—1,4-benzoquinone (BQ), triethanolamine (TEOA), and tertiary butanol (t-BuOH)—were used for demonstrating the significances during the photocatalytic reaction of the active species—superoxide radical ($\bullet O_2^-$), hole (h^+), and hydroxide radical ($\bullet OH$)—respectively. As shown in Figure 11, it is

obvious that $\bullet\text{OH}$ doesn't make any contribution to the photocatalytic performance. Compared with the result without any trapping agents, $\bullet\text{O}_2^-$ has a more significant role than h^+ .

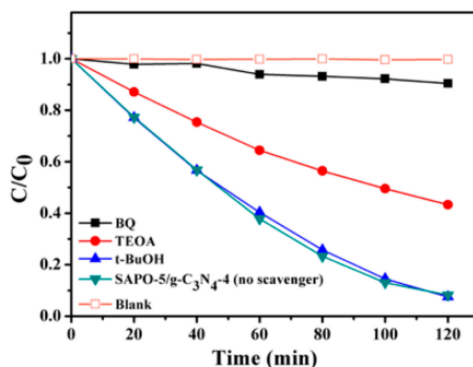
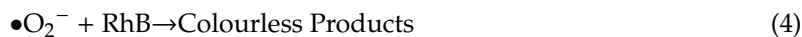
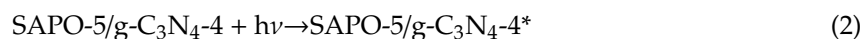
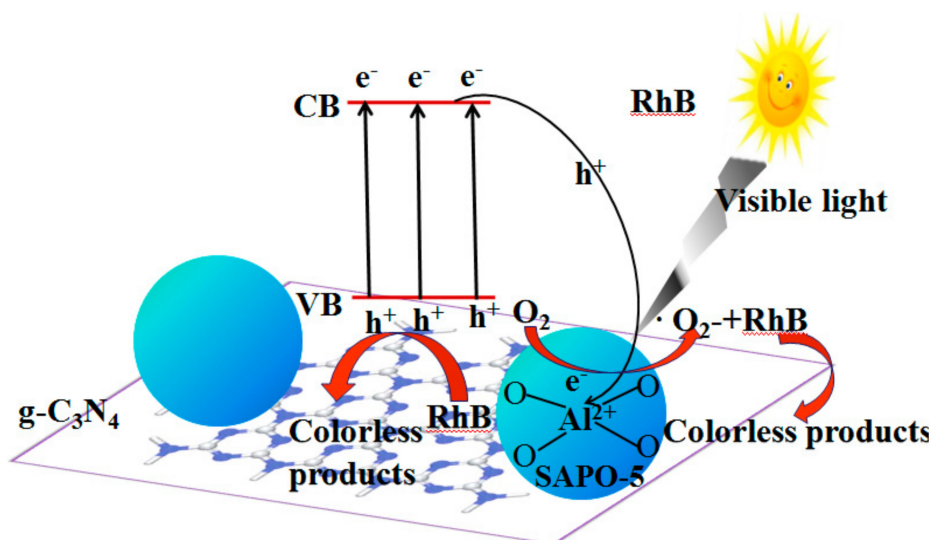


Figure 11. The comparison of the photocatalytic activities of SAPO-5/g-C₃N₄-4 for the degradation of RhB with the addition of BQ, TEOA, t-BuOH, or without scavengers.

The photocatalytic mechanism can be described by Equations (2)–(5), which will be illustrated in detail, as follows. For g-C₃N₄, the electron transmission from the valence band (VB) to the conduct band (CB) will easily happen under visible-light illumination. After SAPO-5/g-C₃N₄-4 composite forms, along with the band gap restructuring, SAPO-5 can also be activated and [Al²⁺-O⁻]^{*} appeared. As described in our previous research, SAPO-5 becomes both of an electron acceptor and an electron donor [12]. The photo-induced electron from the conduction band g-C₃N₄ will migrate to the activated Al sites of SAPO-5, which facilitates the photo-induced electron-hole separation of g-C₃N₄. That is in accordance with the mechanism of the zeolite Y based TiO₂ photocatalyst [27]. Thus, the photocatalytic reaction proceeded at the valence band (VB) of g-C₃N₄ and Al sites in the SAPO-5 framework (Scheme 1). Based on the capture experiments, we can estimate that the RhB molecules were oxidized by the h^+ of g-C₃N₄ and reduced by the $\bullet\text{O}_2^-$ formed by capturing O₂ at Al sites in SAPO-5, respectively.

3.5. Comparison

To further evaluate the significance of the SAPO-5/g-C₃N₄ designed in this work, the photocatalytic performance of SAPO-5/g-C₃N₄ was compared with other g-C₃N₄-based composites applied for organic pollutants (especially for RhB) degradation (Table S3). Considering both the degradation efficiency and apparent rate, SAPO-5/g-C₃N₄ showed promising photocatalytic activity. It provides proof for a bright future of constructing zeolitic material-modified g-C₃N₄ composites in environmental purification.



Scheme 1. The proposed scheme for the separation and transfer of photogenerated charges in SAPO-5/g-C₃N₄-4.

4. Conclusions

In summary, we have successfully prepared SAPO-5/g-C₃N₄ heterojunction-like composites. The effects of the SAPO-5 incorporation proportion in SAPO-5/g-C₃N₄ and pristine RhB concentration on the photocatalytic performance of SAPO-5/g-C₃N₄ has been discussed in detail. As a result, the RhB (30 mg/L) degradation efficiency under the visible light illumination of optimized SAPO-5/g-C₃N₄ is improved by 40.6% compared with that of pure g-C₃N₄. The photocatalytic mechanism of SAPO-5/g-C₃N₄ heterojunction has been proposed. This significant enhancement should be attributed to the heterojunction-like contact between SAPO-5 and g-C₃N₄, which promotes the separation of photo-induced electron-hole pairs in g-C₃N₄. This work opens up new prospects for exploring novel g-C₃N₄/SAPOs heterojunction-like composites with a much higher visible-light photocatalytic performance.

Supplementary Materials: The following are available online at <http://www.mdpi.com/1996-1944/12/23/3948/s1>, Figure S1: UV-vis of RhB degradation by g-C₃N₄ and SAPO-5/g-C₃N₄-4 ([RhB]_{initial}: 10–50 mg/L, catalyst dose: 50 mg, volume: 50 mL, reaction time: 120 min, light source: Xenon lamp, 500 W, λ > 420 nm), Figure S2: UV-vis of RhB degradation by g-C₃N₄ and SAPO-5/g-C₃N₄ composites with different SAPO-5 doping amount ([RhB]_{initial}: 30 mg/L, catalyst dose: 50 mg, volume: 50 mL, reaction time: 120 min, light source: Xenon lamp, 500 W, λ > 420 nm), Figure S3: XRD patterns for fresh SAPO-5/g-C₃N₄-4 and SAPO-5/g-C₃N₄-4 after 5th recycling, Figure S4: SEM image of SAPO-5/g-C₃N₄-4 after 5th recycling. Table S1: g-C₃N₄ and SAPO-5 contents in precursors and SAPO-5/g-C₃N₄ composites, Table S2: Degradation rate constant and cofactor of SAPO-5/g-C₃N₄ samples compared with pure g-C₃N₄, Table S3: Comparison of the photocatalytic dye degradation performance for g-C₃N₄-based binary photocatalysts under visible illumination.

Author Contributions: L.Q.: writing and funding support, study design, literature search; Z.Z.: figures, data collection; M.M.: data collection; P.L.: data analysis and funding support; J.L.: data collection; Y.H.: data collection; X.C.: data analysis, data interpretation; S.D.: study design, funding support.

Funding: This research was funded by National Natural Science Foundation of China (No.41763020), Natural Science Foundation of Jiangxi Province (No.20171BAB206008), Foundation of Jiangxi Educational Commission (No. GJJ180603, No. GJJ180596, and No. GJJ180635), and the Doctoral Scientific Research Starting Foundation of Jiangxi Science and Technology Normal University (No. 2017BSQD003). These foundations are all gratefully acknowledged.

Conflicts of Interest: The authors declare no conflicts of interest.

References

1. Mamba, G.; Mishra, A.K. Graphitic carbon nitride (g-C₃N₄) nanocomposites: A new and exciting generation of visible light driven photocatalysts for environmental pollution remediation. *Appl. Catal. B Environ.* **2016**, *198*, 347–377. [[CrossRef](#)]
2. Kong, L.; Zhang, X.; Wang, C.; Xu, J.; Du, X.; Li, L. Ti³⁺ defect mediated g-C₃N₄/TiO₂ Z-scheme system for enhanced photocatalytic redox performance. *Appl. Surf. Sci.* **2018**, *448*, 288–296. [[CrossRef](#)]
3. Liang, B.; Han, D.; Sun, C.; Zhang, W.; Qi, Q. Deposition of ZnO flowers on the surface of g-C₃N₄ by solid phase reaction. *Funct. Mater. Lett.* **2018**, *11*, 1850020. [[CrossRef](#)]
4. Yan, H.; Cheng, L.; Guo, L. Combination mechanism and enhanced visible-light photocatalytic activity and stability of CdS/g-C₃N₄ heterojunctions. *J. Mater. Sci. Technol.* **2017**, *33*, 30–38.
5. Hosein, B.M.; Kazem, M.; Hadi, S. Preparation and application of a nano α-Fe₂O₃/SAPO-34 photocatalyst for removal of the anti-cancer drug doxorubicin using the taguchi approach. *Chem. Open* **2016**, *14*, 267–273.
6. Bellatreche, S.; Hasnaoui, A.; Boukoussa, B.; García-Aguilar, J.; Berenguer-Murcia, Á.; Cazorla-Amoros, D.; Bengueddach, A. Structural and textural features of TiO₂/SAPO-34 nanocomposite prepared by the sol-gel method. *Res. Chem. Intermediat.* **2016**, *42*, 1–15. [[CrossRef](#)]
7. Anandan, S.; Yoon, M. Photocatalytic activities of the nano-sized TiO₂-supported Y-zeolites. *J. Photoch. Photobio. C* **2003**, *4*, 5–18. [[CrossRef](#)]
8. Rajesh, J.T.; Ramchandra, G.K.; Jasra, R.V. Enhanced photocatalytic activity of TiO₂-coated NaY and HY zeolites for the degradation of methylene blue in water. *Ind. Eng. Chem. Res.* **2007**, *46*, 369–376.
9. Ökte, A.N.; Yilmaz, Ö. Characteristics of lanthanum loaded TiO₂-ZSM-5 photocatalysts: Decolorization and degradation processes of methyl orange. *Appl. Catal. A Gen.* **2009**, *354*, 132–142. [[CrossRef](#)]
10. Zhu, S.; Liang, S.; Ying, W.; Zhang, X.; Li, F.; Lin, H.; Zhang, Z.; Wang, X. Ultrathin nanosheets of molecular sieve SAPO-5: A new photocatalyst for efficient photocatalytic reduction of CO₂ with H₂O to methane. *Appl. Catal. B Environ.* **2016**, *187*, 11–18. [[CrossRef](#)]
11. Xu, X.; Jiang, R.; Shi, H.; Qiang, K.; Wang, P.; Wang, J. Preparation of TiO₂/SAPO-5 composite zeolite and its photocatalytic properties for the degradation of phenol. *J. Adv. Oxid. Technol.* **2016**, *19*, 381–386. [[CrossRef](#)]
12. Qiu, L.; Zhou, Z.W.; Yu, Y.; Zhang, H.; Qian, Y.; Yang, Y.; Duo, S. Fabrication of nanometer-sized high-silica SAPO-5 and its enhanced photocatalytic performance for methyl orange degradation. *Res. Chem. Intermediat.* **2018**, *45*, 1457–1473. [[CrossRef](#)]
13. Liu, Q.; Chen, T.; Guo, Y.; Zhang, Z.; Fang, X. Ultrathin g-C₃N₄ nanosheets coupled with carbon nanodots as 2D/0D composites for efficient photocatalytic H₂ evolution. *Appl. Catal. B Environ.* **2016**, *193*, 248–258. [[CrossRef](#)]
14. Dong, F.; Wu, L.; Sun, Y.; Fu, M.; Wu, Z.; Lee, S.C. Efficient synthesis of polymeric g-C₃N₄ layered materials as novel efficient visible light driven photocatalysts. *J. Mater. Chem.* **2011**, *21*, 15171–15174. [[CrossRef](#)]
15. Wang, L.; Guo, C.; Yan, S.; Huang, X.; Li, Q. High-silica SAPO-5 with preferred orientation: Synthesis, characterization and catalytic applications. *Micropor. Mesopor. Mat.* **2003**, *64*, 63–68. [[CrossRef](#)]
16. Jiang, D.; Wang, T.; Xua, Q.; Li, D.; Meng, S.; Chen, M. Perovskite oxide ultrathin nanosheets/g-C₃N₄ 2D-2D heterojunction photocatalysts with significantly enhanced photocatalytic activity towards the photodegradation of tetracycline. *Appl. Catal. B Environ.* **2017**, *201*, 617–628. [[CrossRef](#)]
17. Ma, T.Y.; Tang, Y.; Dai, S.; Qiao, S.Z. Proton-functionalized two-dimensional graphitic carbon nitride nanosheet: An excellent metal-/label-free biosensing platform. *Small* **2014**, *10*, 2382–2389. [[CrossRef](#)]
18. Wang, X.; Hong, M.; Zhang, F.; Zhuang, Z.; Yu, Y. Recyclable nanoscale zero valent iron doped g-C₃N₄/MoS₂ for efficient photocatalytic of RhB and Cr(VI) driven by visible light. *ACS Sustain. Chem. Eng.* **2016**, *4*, 4055–4063. [[CrossRef](#)]
19. Liu, C.; Zhang, Y.; Dong, F.; Du, X.; Huang, H. Easily and synchronously ameliorating charge separation and band energy level in porous g-C₃N₄ for boosting photooxidation and photoreduction ability. *J. Phys. Chem.* **2016**, *120*, 10381–10389. [[CrossRef](#)]
20. Bayan, S.; Gogurla, N.; Midya, A.; Ray, S.K. White light emission characteristics of two dimensional graphitic carbon nitride and ZnO nanorod hybrid heterojunctions. *Carbon* **2016**, *108*, 335–342. [[CrossRef](#)]
21. Jiang, D.; Yu, H.; Yu, H. Modified g-C₃N₄/TiO₂ nanosheets/ZnO ternary facet coupled heterojunction for photocatalytic degradation of p-toluenesulfonic acid (p-TSA) under visible light. *Physica E* **2017**, *85*, 1–6. [[CrossRef](#)]

22. Wei, X.L.; Lu, X.H.; Zhang, T.J.; Chu, X.; Zhou, D.; Nie, R.F.; Xia, Q.H. Synthesis and catalytic application of SAPO-5 by dry-gel conversion for the epoxidation of styrene with air. *Microp. Mesop. Mater.* **2015**, *214*, 80–87. [[CrossRef](#)]
23. Singh, A.; Yadav, R.; Sudarsan, V.; Kishore, K.; Upadhyayula, S.; Sakthivel, A. Mesoporous SAPO-5 (MESO-SAPO-5): A potential catalyst for hydroisomerisation of 1-octene. *RSC Adv.* **2014**, *4*, 8727–8734. [[CrossRef](#)]
24. Miao, X.L.; Shen, X.P.; Wu, J.J.; Ji, Z.Y.; Wang, J.H.; Kong, L.R.; Liu, M.M.; Song, C.S. Fabrication of an all solid Z-scheme photocatalyst g-C₃N₄/GO/AgBr with enhanced visible light photocatalytic activity. *Appl. Catal. A Gen.* **2017**, *539*, 104–113. [[CrossRef](#)]
25. Bharat, L.K.; Nagaraju, G.; Krishna, K.G.; Yu, J.S. Controlled synthesis of yttrium gallium garnet spherical nanostructures modified by silver oxide nanoparticles for enhanced photocatalytic properties. *Crystengcomm.* **2016**, *18*, 8915–8925. [[CrossRef](#)]
26. Qi, C.; He, Q.; Lv, M.; Liu, X.; Jin, W.; Lv, J. The vital role of PANI for the enhanced photocatalytic activity of magnetically recyclable N-K₂Ti₄O₉/MnFe₂O₄/PANI composites. *Appl. Surf. Sci.* **2014**, *311*, 230–238.
27. Dubey, N.; Rayalu, S.S.; Labhsetwar, N.K.; Naidu, R.R.; Chatti, R.V.; Devotta, S. Photocatalytic properties of zeolite-based materials for the photoreduction of methyl orange. *Appl. Catal. A Gen.* **2006**, *303*, 152–157. [[CrossRef](#)]



© 2019 by the authors. Licensee MDPI, Basel, Switzerland. This article is an open access article distributed under the terms and conditions of the Creative Commons Attribution (CC BY) license (<http://creativecommons.org/licenses/by/4.0/>).